

Supplement of The Cryosphere, 15, 265–282, 2021
<https://doi.org/10.5194/tc-15-265-2021-supplement>
© Author(s) 2021. This work is distributed under
the Creative Commons Attribution 4.0 License.



Supplement of

Debris cover and the thinning of Kennicott Glacier, Alaska: in situ measurements, automated ice cliff delineation and distributed melt estimates

Leif S. Anderson et al.

Correspondence to: Leif S. Anderson (leif.anderson@unil.ch)

The copyright of individual parts of the supplement might differ from the CC BY 4.0 License.

Supplementary Materials

S1 In situ measurements

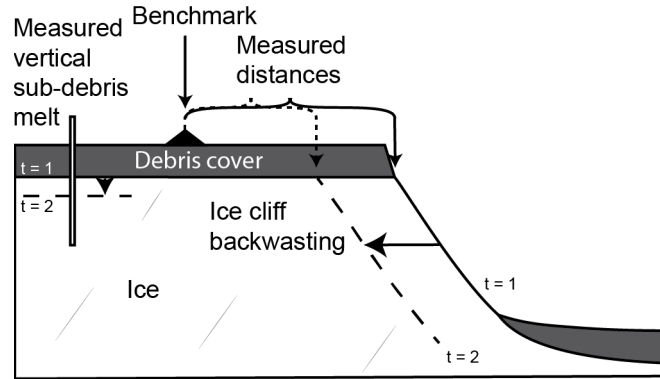


Fig. S1 Schematic of sub-debris melt rate and ice cliff backwasting rate measurements.

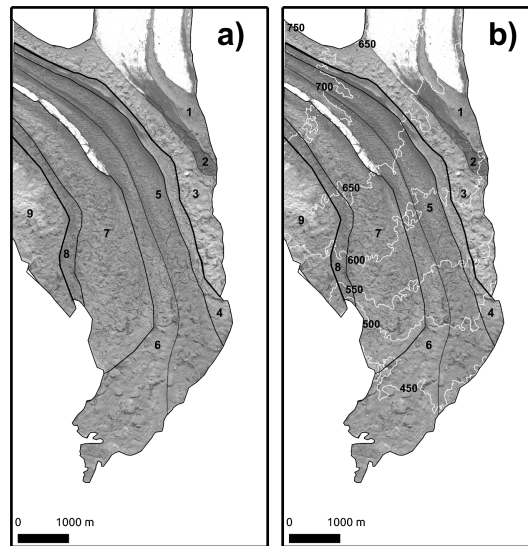


Fig. S2 High-resolution orthoimage with medial moraines delineated. WorldView image from 13 July 2009 (catalog ID: 1020010008B20800) is shown in both panels. a) Image with medial moraines delineated and labeled. b) Image with medial moraines delineated, labeled, and with elevation contours from 2013. 69 % of debris thickness measurements are from medial moraines 5-7. A trail up the east side of the glacier allowed easy access to medial moraines 1, 2, and 3. More data is collected there than on the west side of the glacier. Note the light color debris in medial moraine 9, which is debris in excess of ~1 m thick.

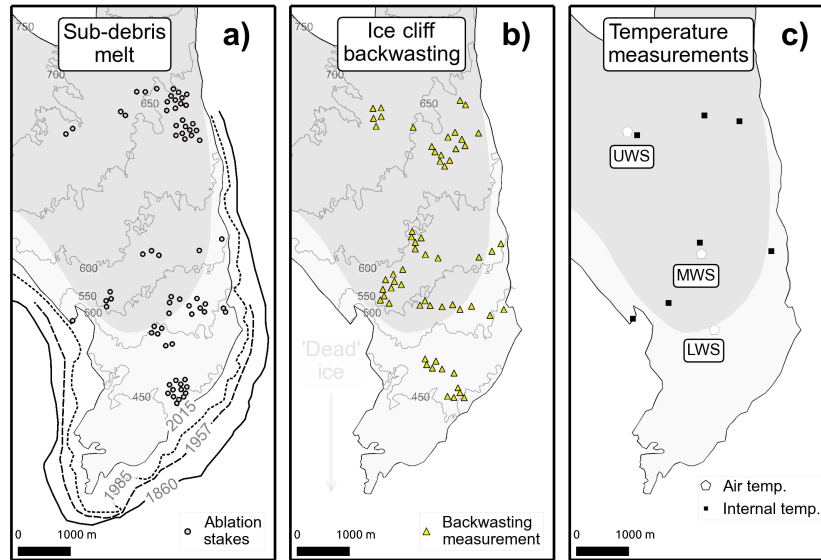


Fig. S3 Map of the general study area with in situ measurement locations. a) Locations of sub-debris melt rate measurements. Map of the study area with contours derived from 2013. b) Locations where ice cliff backwasting was measured. The ice extents are derived from WV imagery and aerial photos. The ‘dead’ ice portion of the debris-covered tongue is shown in light grey. It is defined by areas that only have measured daily mean surface velocities above 5 cm d^{-1} (Armstrong et al., 2016). This definition coincides with the definition of ‘dead’ ice from Rickman and Rosenkrans (1997). c) Location of air temperature poles and internal debris temperature profiles. The letters label the air temperature poles: Upper weather station (*UWS*); Middle weather station (*MWS*); Lower weather station (*LWS*).

S1.1 Sub-debris melt rates

We measured sub-debris melt at 74 locations (Fig. S3). Sub-debris melt (\dot{b}_{debris}) was measured by removing the debris and measuring ice surface lowering (Fig. S1).

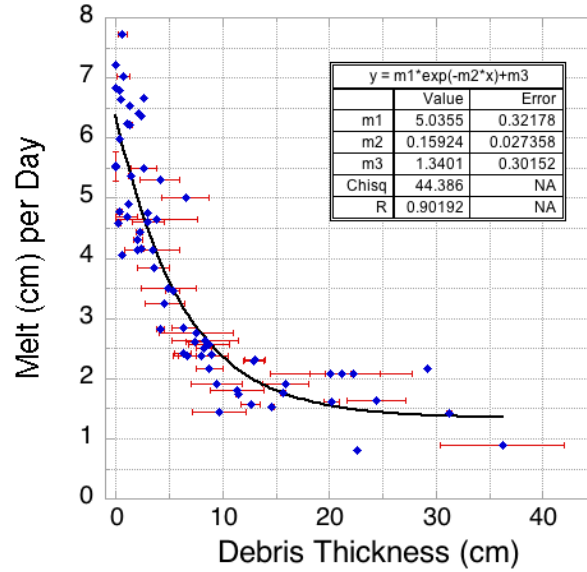


Fig. S4 Error in debris thickness measurements plotted with sub-debris melt. Error bars for debris thickness represent changes upon repeated measurement. An exponential fit is shown here though we do not use this curve fit elsewhere.

Because melt measurements were made over different time periods we corrected each measurement to represent the full measurement period between 18 June and 16 August 2011. A degree-day factor for sub-debris melt DDF_{debris} was therefore calculated for each sub-debris melt measurement:

$$DDF_{debris} = \frac{\sum_{i=1}^n \dot{b}_{debris}}{\sum_{i=1}^n T^+ \Delta t} \quad (S1)$$

where T^+ is the positive degree-days defined as the mean daily air temperature when above 0°C and Δt is one day (e.g., Hock, 2003). Air temperatures did not drop below freezing during the study period. We use hourly air temperature data from the Gates Glacier and May Creek meteorological stations to estimate the T^+ at each site. Gates Glacier meteorological station is located at 1240 m a.s.l. and May Creek meteorological station is located 15 km to the southwest of McCarthy at 490 m a.s.l. (Figure 1, main text). The average period between measurements was 24 days, the minimum was 8 days, and the maximum was 56 days. Sub-debris melt rates presented in the main paper have had this correction applied, but ultimately this correction exceptionally small. The correction has a negligible effect on the curve fit applied to the distributed estimates of melt, but we correct for the measurement period nonetheless (Fig. S5).

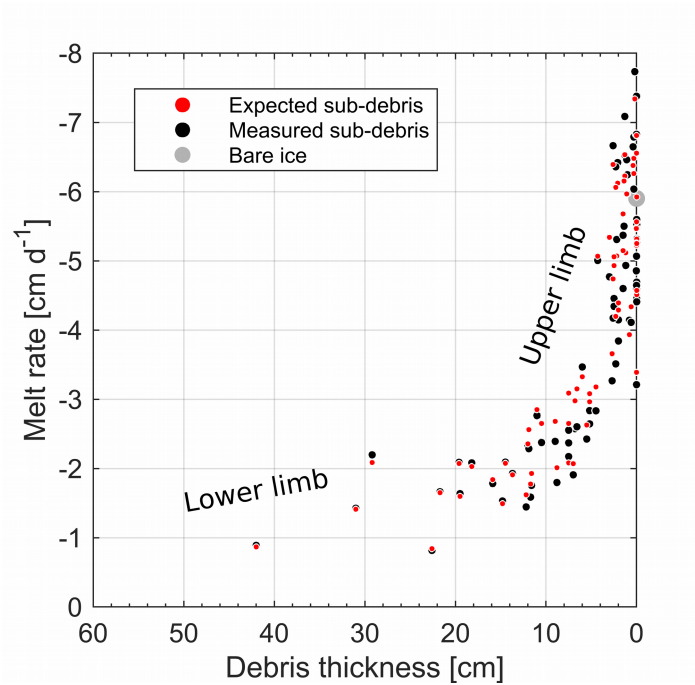


Fig. S5 Difference between measured melt rates and expected melt rates (those corrected to the full study period) with debris thickness. The root mean squared difference between the measured and expected melt rates is 0.5 [cm d⁻¹].

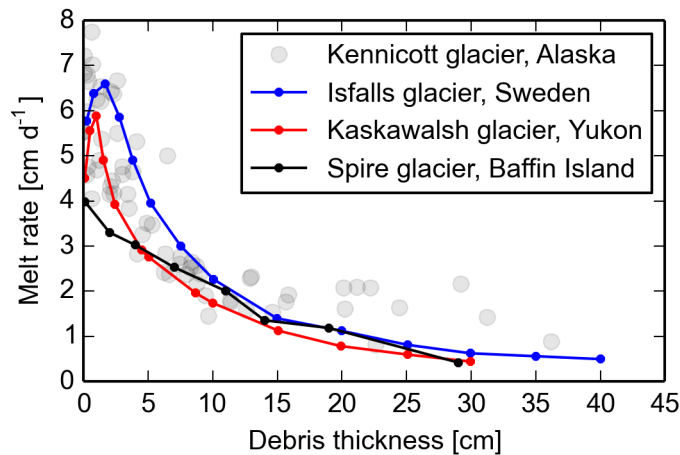


Fig. S6 Comparison between Kennicott (61.5° N) sub-debris melt rates and other glaciers at similar latitudes.

Isfallsgläciären (67.9° N; Østrem, 1959), Kaskawalsh Glacier (60.8° N; Loomis, 1970), Spire Glacier (66.4° N; Crump et al., 2017).

Measured sub-debris melt rates follow the typical shape of Østrem's curve from other glaciers at similar latitudes (Fig. S6). But sub-debris melt rates are higher for debris thicknesses greater than 15 cm, than on other debris-covered glaciers at similar latitudes. This discrepancy could be explained by the variability of air temperature within the study area: we measured sub-debris melt across a 250 meter elevation range, and most melt measurements under thick debris were derived from the lowest portion of the study area. This difference could also reflect the proportion of fine material making up the thicker debris cover downglacier (e.g., Owen et al., 2003). Juen et al. (2013) demonstrated that increasing the proportion of fine material in debris covers increases water retention, ultimately increasing debris thermal conductivity and hence melt rates.

S1.2 Ice cliff backwasting rates

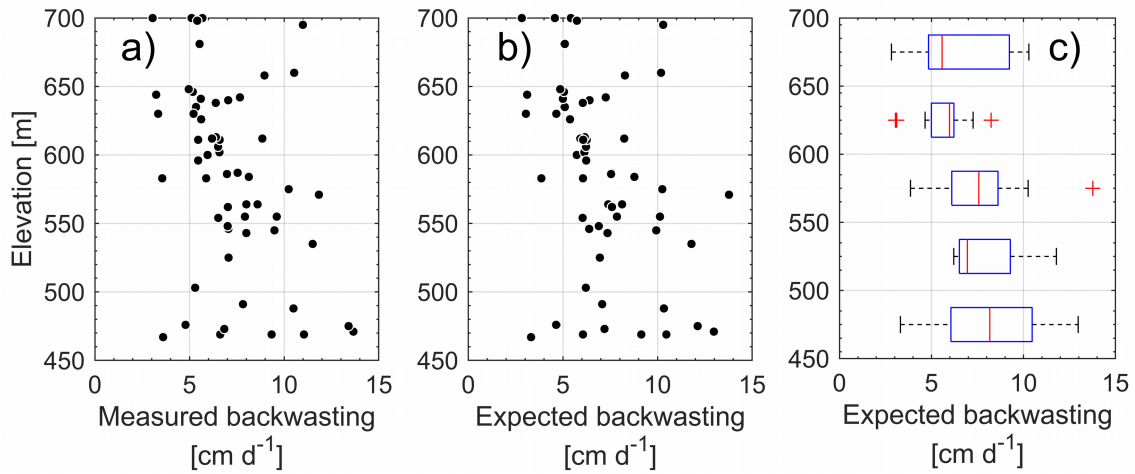


Fig. S7 Pattern of ice cliff backwasting as it varies with elevation. a) Measured ice cliff backwasting over different time intervals. b) Ice cliff backwasting corrected to the full measurement period using the individual degree-day factor for each ice cliff using equation S1 but for backwasting instead of sub-debris melt. Note the minor effect of the correction. The mean of these data is 7.05 cm d^{-1} and the standard deviation is 2.46 cm d^{-1} . c) Expected backwasting boxplots in 50 meter elevation bins. Outliers are represented as '+'s.

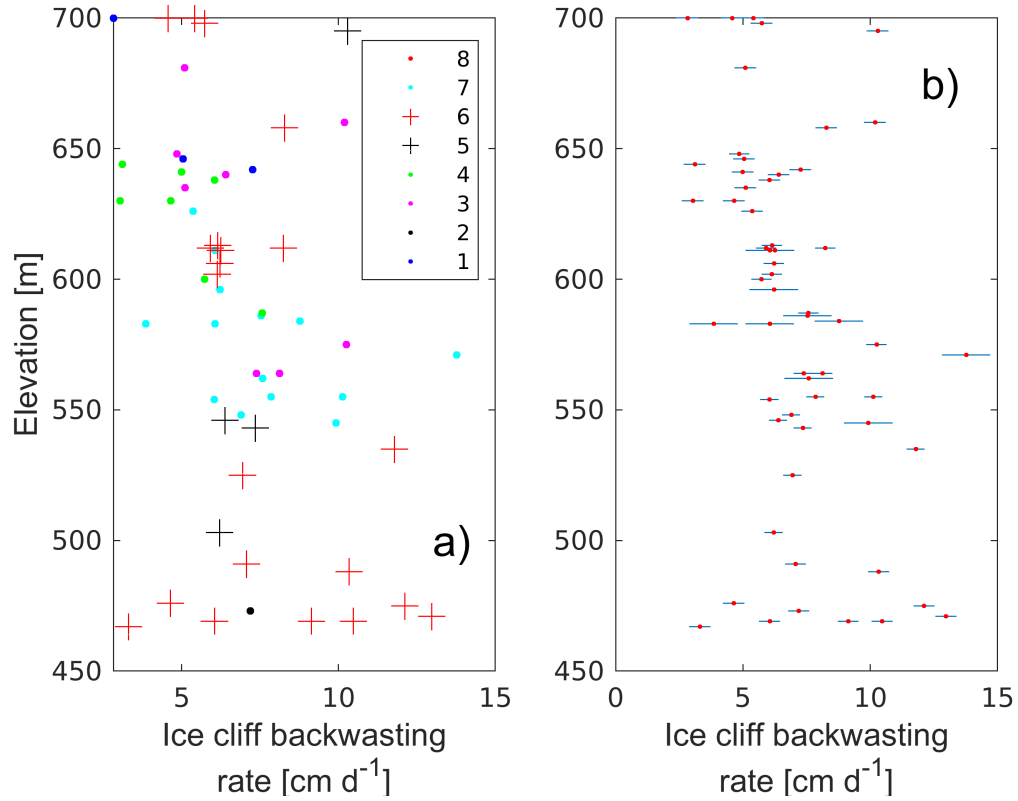


Fig. S8 Ice cliff backwasting rate as it varies with elevation and medial moraine. a) Medial moraine #9 is the medial moraine furthest to the west in the study area and 1 is the eastern most medial moraine at the end of Root Glacier. Note that no backwasting measurements were made on medial moraine 2. There are not clear trends in backwasting rate with medial moraine. b) Ice cliff backwasting rates with error bars based on a measurement uncertainty of ± 20 cm per distance measurement.

S1.3 Mean ice cliff slopes

In establishing the uncertainty in our distributed melt estimates we need to determine the plausible uncertainty in mean ice cliff slope across the study area. In order to estimate this uncertainty we compiled all studies that present a measured mean ice cliff slope (for the population of ice cliffs analyzed in the specific study).

Table S1 Compilation of mean ice cliff slopes for the respective population

Glacier Name	Region	Reference	Mean ice cliff slope
Changri Nup	Himalaya, Nepal	Brun et al., 2018	47.4°
Lirung	Himalaya, Nepal	Brun et al., 2016	45°
Langtang	Himalaya, Nepal	Kraaijenbrink et al., 2016	44.6°
Khumbu	Himalaya, Nepal	Watson et al., 2017	59°
Koxkar	Tien Shan, China	Han et al., 2010	46.4°
Miage	European Alps, Italy	Reid and Brock, 2014	50.7°
Kennicott	Wrangell Mtns, Alaska	This study	48°

* the mean of mean ice cliffs slopes including the Kennicott data is 48.7° with a standard deviation of 4.7°

S1.4 Near-surface air temperature

Boundary layer conditions differ between debris-free and debris-covered glaciers (e.g., Brock et al., 2010). This is primarily due to differences in surface temperature between debris-free and debris-covered glacier surfaces. During the melt season, debris-free surface temperatures are typically near the melting point. But debris surface temperatures vary strongly with debris thickness and surface topography (e.g., Shaw et al., 2016).

We installed three air temperature poles (Fig. 2; at 513, 600, and 704 m a.s.l.) to document the interplay between debris, air temperature, and surface melt across the study area. Air temperatures were measured hourly between July 21 and August 9, using iButton thermistors in standard HOBO radiation shields. Poles were partially drilled into the ice and then debris 30 cm thick was accumulated around the pole in a 1 meter radius. Thermistors were initially placed 1.8 m above the debris surface. Thermistors were moved back to their original elevation above the debris surface in the middle of station deployment. The maximum deviation of thermistors from the original height above the surface was 14 cm. The thermistors have a measurement uncertainty of 0.5 °C based on ice bath calibration. We refer to the individual temperature poles as the Lower, Middle, and Upper weather stations (*LWS*, *MWS*, *UWS*). Unperturbed debris thicknesses averaged 2 cm at the *UWS*, 10 cm at the *MWS*, and 22 cm at the *LWS*. The *UWS* and *MWS* were placed in areas with lower surface relief while the *LWS* was located near the base of a topographic bulge.

Fig. S9 shows data from the *LWS* as well as near-surface air temperature lapse rates. Lapse rates between *LWS* and *MWS* were extremely steep, up to -74 C km^{-1} , with a mean lapse rate of -25 C km^{-1} over the measurement period (Table S2). Lapse rates were more shallow between the *MWS* and *UWS*, with a mean of -7.3 C km^{-1} , more typical of lapse rates above debris cover (-7.5 C km^{-1} , Mihalcea et al., 2006; -8.0 and -6.7 C km^{-1} , Brock et al., 2010; -5 to -7.8 C km^{-1} , Steiner and Pellicciotti, 2016).

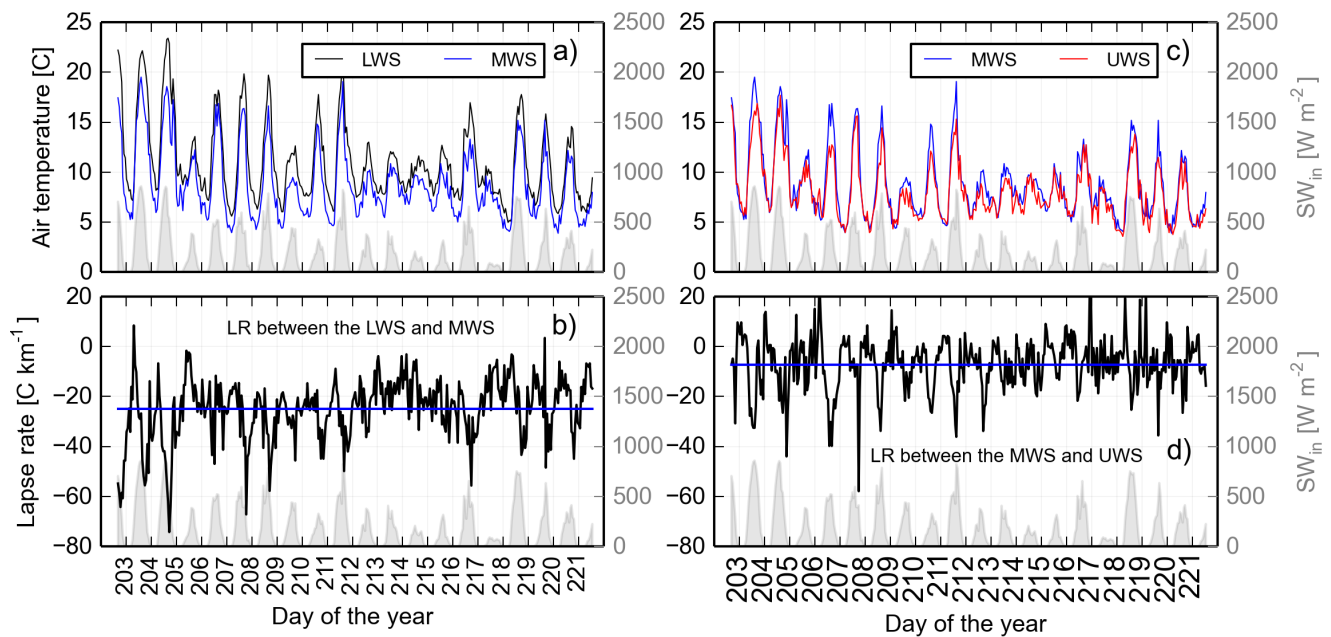


Fig. S9 Air temperature and near-surface air temperatures lapse rate within the study area. a) Screen-level air temperature data from Lower weather station (*LWS*), Middle weather station (*MWS*), and incoming shortwave radiation data from the May Creek meteorological station. b) Lapse rate between *LWS* and *MWS* with May Creek shortwave radiation. c) Screen-level air temperature from *MWS*, Upper weather station (*UWS*), and incoming shortwave radiation data recorded from May Creek meteorological station. d) Lapse rate between *MWS* and *UWS* with May Creek shortwave radiation.

Table S2. Near-surface air-temperature lapse rates within the study area

Near-surface air temperature lapse rate [C km ⁻¹]	Mean [C km ⁻¹]	1 St. dev. [C km ⁻¹]	Day [C km ⁻¹]	Night [C km ⁻¹]	Estimated debris surface temperature difference on clear-sky day [C]
Lower-Middle	-25.2	12.8	-30.0	-22.8	24
Middle-Upper	-7.30	10.4	-13.7	-3.90	2
Lower-Upper	-15.4	8.50	-21.1	-7.20	26
May Creek – Gates Glacier	-5.59	3.98	-8.95	-3.85	-

*Lower, Middle, and Upper air temperature poles are on the glacier, May Creek and Gates Glacier stations are off-glacier.

**Estimated debris surface temperatures based on clear sky days using a Fluke Infrared Thermometer.

The study area is spanned by off-ice meteorological stations, which are typically used for estimating melt on glacier surfaces (Figure 1, main text). For comparison, lapse rates calculated between these off-ice meteorological stations were a more typical -5.6 C km^{-1} (e.g., Minder et al., 2010).

Lapse rates tended to be steeper during the afternoon and evening than the night and morning (Table S2 and Fig. S9). An observation similar to those of Fujita and Sakai (2000) and Steiner and Pellicciotti (2016) on Lirung Glacier, Nepal and Brock et al. (2010) and Shaw et al. (2016) on Miage Glacier, Italy. The steepest lapse rates occurred between 5 and 7 pm. Steep lapse rates in the afternoon and evening are likely caused by higher debris surface temperatures, and convective heating at lower elevations. The daily-lapse rate cycle was amplified on clear-sky days (Fig. S9; e.g., day-of-the-year (DOY) 203 and 204 compared to DOY 212-215).

Variable, steep lapse rates occurred on clear-sky days, while lapse rates were less variable and shallower on cooler, cloudy days. Amplified debris surface temperatures, as well as a decreased sky-view (see Steiner and Pellicciotti, 2016) at *LWS* may explain the extreme temperature differences between *LWS* and *MWS*. *UWS* and *MWS* are more likely to be influenced by cold-air drainage from up valley. Because debris is thicker at *LWS* debris surface temperatures will also tend to be higher. These extreme air temperature differences highlight the need for further study of the relationship between debris, surface temperature, and air temperature variations on debris-covered glaciers.

On sunny days, a steep air temperature lapse rate is observed above the debris. The extreme lapse rates observed in the lower portion of the study area are likely caused by feedbacks related to debris thickness. On clear days, high direct solar radiation fluxes increase debris surface temperatures for debris thicker than ~20 cm much more than for thinner debris. Debris thicknesses at *LWS* are in the range where debris surface temperatures rapidly increase with debris thickness. In contrast, at *MWS* and *UWS*, debris thicknesses were only 10 and 2 cm, respectively. This suggests that strong gradients in air temperature may be related to feedbacks between debris thickness and surface temperature. The steep lapse rates could also be related to the large areas of exposed ice above the debris-covered tongue. The upper stations are more likely to be affected by descending katabatic winds. Air temperatures at the *LWS* may also be affected by the local debris-covered topography (e.g., Shaw et al., 2016).

S1.5 Debris thermal properties

In order to constrain debris thermal properties, thermistors were placed within the debris at ten sites. At each site, three to four iButton thermistors were placed in vertical profile within the debris. All profiles were paired with nearby ablation stake measurements. Temperature was measured every 30 minutes and each profile was in debris for at least one week, allowing for an assumption of a linear temperature gradient through the debris (e.g., Conway and Rasmussen, 2000; Fig. S10). Thermistors were placed in debris between 8 and 46 cm thick, in four medial moraines composed of distinct lithological combinations. The debris cover is composed of sedimentary and volcanic rocks, including: andesite, pyroclastics, dacite, limestone, greenstone, and shale (MacKevett, 1972; MacKevett and Smith, 1972). We estimated debris conductivity using simultaneous measurements of sub-debris melt, internal debris temperature, and debris thickness (e.g., Nakawo and Young, 1981, 1982; Kayastha et al., 2000; Mihalcea et al., 2006). The heat flux (Q_m) is proportional to the effective thermal conductivity (K_e) of the debris for a given temperature gradient, which is set largely by surface temperature (T_s) due to the nearly constant 0° C summertime temperature of melting ice (T_i):

$$Q_m = K_e \frac{(T_s - T_i)}{h_{debris}}, \quad (S2)$$

where h_{debris} is debris thickness. The modifier *effective* is used to emphasize that heat is also transferred by advection of air and water (e.g., Juen et al., 2013). The sub-debris melt rate (per unit area) is related to the energy available for ablation (Q_m) through:

$$Q_m = L_f \rho_i a, \quad (S3)$$

where L_f is the latent heat of fusion of ice ($334 \times 10^3 \text{ J kg}^{-1}$), ρ_i is the density of ice (900 kg m^{-3}), and a is the sub-debris melt rate (m d^{-1}). We estimated mean debris surface temperatures at each site by linearly extrapolating mean internal debris temperatures. Using Eq. (S2 and S3), we then calculate K_e for each temperature profile over the entire duration of the temperature measurements (Fig. S11).

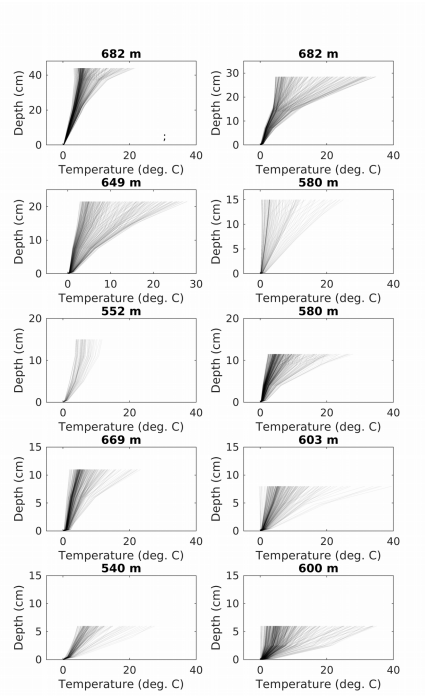


Fig. S10 Debris internal temperatures as they vary in time. The elevation where each profile was located is shown in the title. The uncertainty of each temperature measurement is ± 0.5 deg. C. Uncertainties associated with the measurement of thermistor depth are shown in Fig. S12.

Debris thermal conductivity ranged from 0.525 to $2.16 \text{ W (m C)}^{-1}$ with a mean of $1.06 \text{ W (m C)}^{-1}$ (Figs. S11 and S12). Our estimates broadly agree with the range of previous direct measurements of K_e from debris-covered glaciers (0.85 to 2.6 W (m C)^{-1} ; Nakawo and Young, 1982; Conway and Rasmussen, 2000; Juen et al., 2013). The measurements are also within the range of K_e estimated from physical constants (0.47 to $1.97 \text{ W (m C)}^{-1}$; Nicholson and Benn, 2006).

Debris thickness appears to be a primary control of debris conductivity, even though the thermistor profiles were placed in debris composed of distinct lithological mixes. Perhaps the increase in thermal properties with debris thickness reflects a decrease in porosity as debris thickens. Thicker debris covers tend to have increased fine material at depth (e.g., Owen et al., 2003), which tends to reduce porosity. If little air convection occurs in the pores of the thinner, higher porosity debris then the bulk K_e would be greatly reduced due to the low thermal conductivity of air relative to rock (as described by Juen et al., 2013).

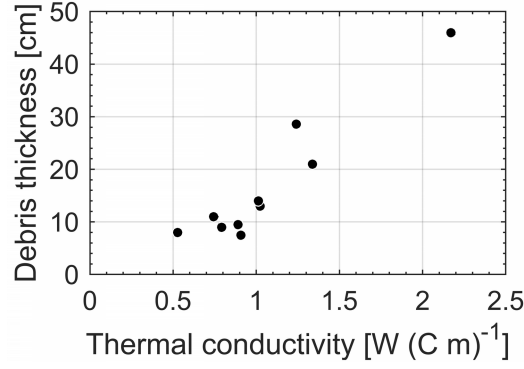


Fig. S11 Thermal conductivity of the debris cover. Effective thermal conductivity (K_e) as it varies with debris thickness. Estimates are based on internal debris temperatures and sub-debris melt measurements over at least a week.

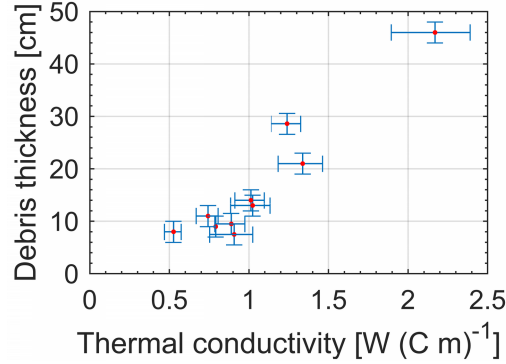


Fig. S12 Thermal conductivity of the debris cover with error bars based on thermistor measurement uncertainty and debris thickness uncertainty.

S1.6 Bare-ice melt rates extrapolated across the study area

For reference we also estimate the bare-ice melt rate through the study area for the summer of 2011, in the hypothetical case that no debris was present on the glacier. We calculate the bare-ice degree-day factor from several ablation stakes in bare-ice in the northeastern portion of the study area. We calculate the degree-day factor for ice (e.g., Hock, 2003) DDF_{ice} using measured bare-ice ablation (\dot{b}_{ice}) and air temperatures interpolated across the glacier:

$$DDF_{ice} = \frac{\sum_{i=1}^n \dot{b}_{ice}}{\sum_{i=1}^n T^+ \Delta t} \quad (S4)$$

where T^+ is the positive degree-days defined as the mean daily air temperature when above 0°C and Δt is one day. Air temperatures did not drop below freezing during the study period. We use hourly air temperature data from the Gates Glacier and May Creek meteorological stations to estimate the T^+ at each measurement location. We do not use air temperature measurements from the glacier surface because they are not necessarily representative of the ~ 1 km of the atmosphere above the glacier (e.g., Ohmura, 2001), our near-surface air temperature measurements do not span the full

study period. Our intention is to show what bare-ice melt rate we might expect if surface debris did not perturb boundary layer air temperature. For all these reasons off-glacier meteorological stations are better for estimating hypothetical bare-ice melt rates within the study area. On-glacier positive degree-days were calculated based on off-glacier meteorological stations. The mean bare-ice degree-day factor was then used to calculate bare-ice melt rates across the study area.

S2 Automatic ice cliff detection

Table S3 Optimal image processing parameters for ice cliff delineation in the July 2009 WorldView scene, as determined by a Monte Carlo method.

Adaptive binary threshold (ABT)	Min brightness [DN*]	Max brightness [DN]	Window size [px]	Brightness offset [DN]	Opening kernel size [px]
	20	42	267	52	3
Sobel edge detection (SED)	Min brightness [DN]	Max brightness [DN]	Threshold gradient [DN px ⁻¹]	Opening kernel size [px]	
	32	55	22	4	

*DN = digital number, a 0-255 representation of relative radiance of each pixel.

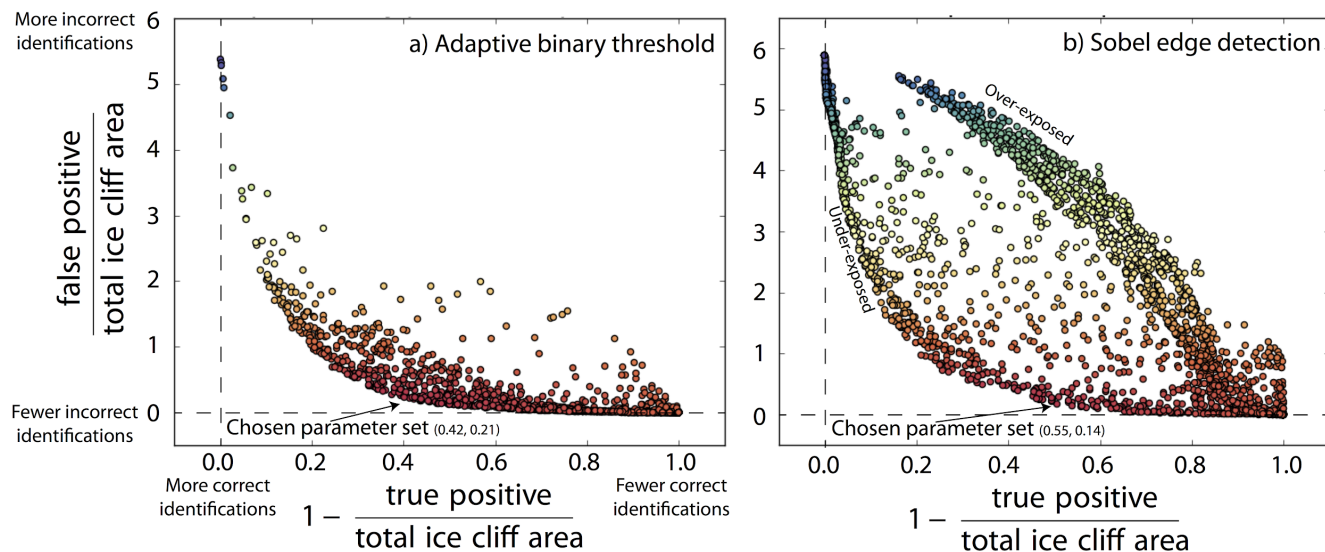


Fig. S13 Parameter optimization for a) adaptive binary threshold (ABT) and b) sobel edge detection (SED) ice cliff detection algorithms. On each plot, every point represents algorithm ice cliff detection error averaged across twelve manually digitized zones. The horizontal axes show true positives (i.e., automated and hand-digitized ice cliffs agree) and vertical axes show false positives (i.e., automated method predicts ice cliff where none exists). Perfect algorithm performance would plot on the origin. The coordinates for our chosen parameter sets provide an estimate of the error associated with the method. Note the differing axis limits on the horizontal and vertical axes. Markers are colored by Euclidean distance from the origin.

S3 Additional distributed melt estimates

For all explorations in the main text and supplementary materials the summer 2011 melt rate is not maximized in the zone of maximum thinning (*ZMT*) (Table S4). Below we show how distributed melt estimates vary depending on the debris thickness assumed for medial moraine #9; we show more extreme uncertainty bounds for the best case shown in the main text; 3) we apply a linear backwasting rate, that varies with elevation; 4) we apply linear curve fits through the debris thickness from each medial moraine; and 5) we apply a single sigmoidal curve fit through all applicable debris thickness data.

Table S4. Comparison of addition uncertainty cases

Case	% contribution of ice cliffs in the study area	Factor increase in melt (ice cliff + sub-debris) to match hypothetical bare ice rates in <i>ZMT</i>
Piecewise w/ center sigmoid (best case)	26 (20 , 40)	2.48 (4.4, 1.6)
h_{debris} in medial moraine #9 reduced by 50% (best case)	25 (19, 39)	2.46 (4.3, 1.6)
Elevation dependent backwasting (best case)	25.4 (19, 37)	2.4 (4.4, 1.6)
Piecewise-individual moraines linear fit	29 (19, 39)	2.35 (4.2, 1.6)
Single sigmoidal curve fit across all medials	24 (11, 50)	2.58 (6.5, 1.2)

* (best case) means that in this case all parameters and assumptions are the same for the ‘best case’ except for the change indicated in the table.

**Extreme bounds are in the parentheses.

S3.1 Distributed debris thicknesses based on elevation and medial moraine

S3.1.1 ‘Best case’ in main text (Piecewise sigmoidal and linear curve fits)

In the main text we extrapolate debris thickness across the 9 medial moraines in a piecewise fashion (Fig. S14). For the 5 central medial moraines we apply the elevation dependent sigmoidal curve fit to all debris-designated pixels across these 5 medial moraines (Fig. 5). For medial moraines with debris thicknesses that do not show a sigmoidal debris thickness-melt relationship we apply linear curve-fit:

$$h_{debris} = m * z + n \quad , \quad (S5)$$

where m is the slope, z is the elevation, and n is the y-intercept.

For medial moraine #9 on the far western portion of the glacier, where access was difficult, we apply a uniform debris thickness across the medial moraine area (Fig. S14). Some debris thickness measurements were made at the very lowest portion of the medial moraine but they are not representative of the upper part of the moraine. North and west of the study

area debris thicknesses greater than 1 m were observed on medial moraine 9 in a portion of the glacier of similar character to the light colored debris presented in Fig. S2. This medial moraine also shows no ice cliffs in its upper reaches within the study area (Fig. S2). We set the mean debris thickness to 20 cm and the interquartile range to 20 cm.

For the five central medial moraines debris thickness uncertainties are based on the interquartile range as it varies in 50 m elevation bins. For the other medial moraines, the uncertainty is based on the interquartile range for all debris thickness measurements made within the medial moraine. Note that we anecdotally saw similar debris thicknesses between medial moraine # 8 and the other central 4 medial moraines. For this reason we include it with the other central medial moraines.

The ‘best case’ distributed melt rate estimates are presented in Figure 12 of the main text. We also present uncertainty estimates with ± 2 -sigma bounds applied to backwasting rate, mean ice cliff slope, and sub-debris melt (Fig. S15). In this case for the sub-debris + ice cliff melt 99.996% of estimates are inside of the red band in Figure S15.

Our approach assumes that small-scale debris thickness variability has a negligible effect on area-averaged melt rates, despite the non-linear debris-melt rate relationship. Including small-scale variability in debris thickness cannot decrease the *effective* debris thickness (therefore increasing local melt) below the minimum in situ measured debris thickness in any given elevation band. We see from Figure 5 that the minimum measured debris thicknesses are much larger in the *ZMT* than immediately above the *ZMT*. Small-scale variability in debris thickness therefore cannot lead to a peak in melt rates in the *ZMT*. It is also highly likely that the range of plausible effects from small-scale debris variability lie within extreme sensitivity tests as described in this and sections 4.4, and S3.1, further suggesting that this assumption is unlikely to affect our conclusions.

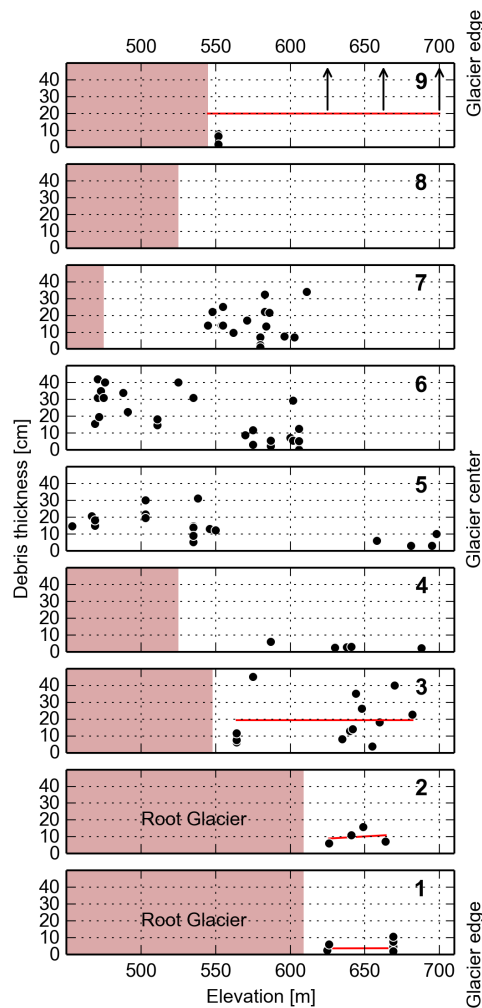


Fig. S14 Debris thickness measurements for each medial moraine in the study area. Shaded brown areas are off glacier such that the white in the figure indicates that the medial moraine exists at that elevation. For moraine # 9 the light area has very thick debris likely over 1 m thick. A survey found that debris was greater than 1 m just above the study area. We assign a most likely debris thickness to this moraine of 20 ± 10 cm for the base case, shown in the main text. We test this assumptions' affect on the uncertainty estimates below. The middle five panels are used for the sigmoidal curve fit shown in the main paper. The red lines in the panels near the glacier margin show the linear curve fits applied to those medial moraines. Note that the lower two panels are on Root Glacier, where it joins Kennicott Glacier. Because of its accessibility from the glacier margin measurements were also taken from these medial moraines.

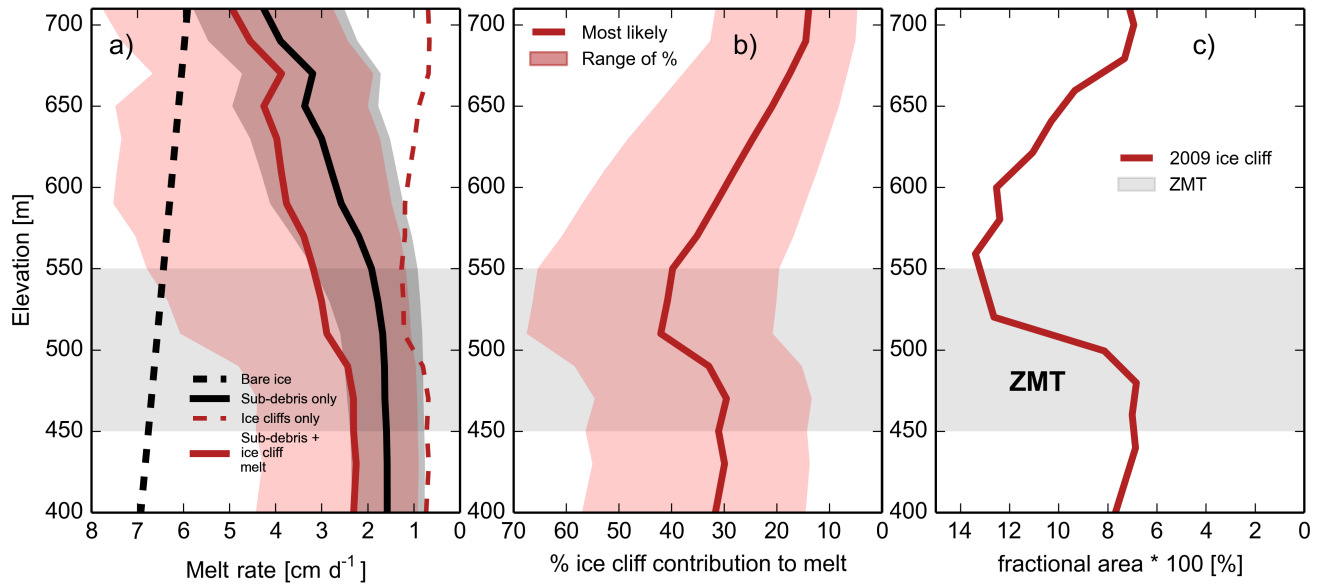


Fig. S15 The best distributed melt rate estimate with ± 2 st. dev. bounds applied to backwasting rate, mean ice cliff slope, and sub-debris melt. a) For the sub-debris melt estimates, 96.8 % of estimates are within the grey band. For sub-debris + ice cliff melt 99.996% of estimates are inside of the red band. b) The percent contribution of ice cliffs to mass loss (sub-debris + ice cliff) with elevation. The red band contains the extreme range of melt contributions from ice cliffs. c) The fractional area of ice cliffs.

S3.1.2 Exploring the mean thickness of moraine #9 in the ‘best case’

Here, we explore reducing the assumed mean debris thickness in medial moraine #9 by 50%. The mean debris thickness applied is 10 cm instead of 20 cm as it is in the best case. The uncertainty bounds use debris thicknesses of 5 and 15 cm as compared to 10 and 30 cm uncertainties for the ‘best case.’ The difference between this case and the original ‘best case’ is small (Table S3).

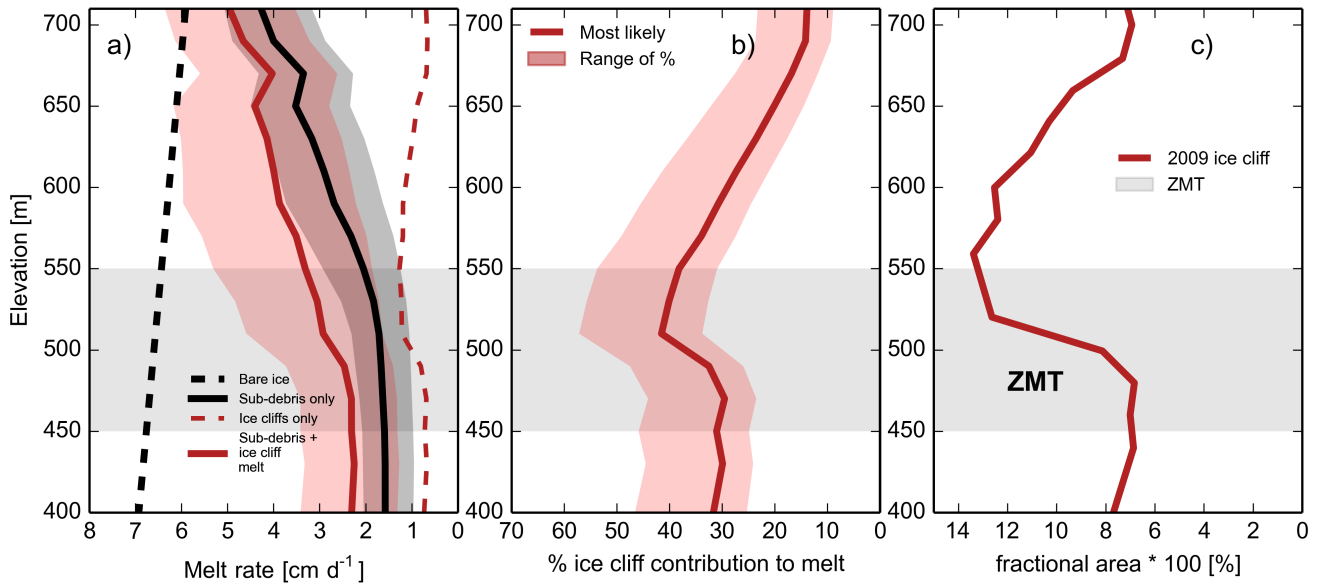


Fig. S16 The best distributed melt rate estimate with the debris thickness medial moraine #9 halved. ± 1 st. dev. bounds are applied to backwasting rate, mean ice cliff slope, and sub-debris melt. The red band contains an extreme range of sub-debris plus ice cliff melt based on compounding parameter choices such that 98.4 % of estimates lie within it (see section 2.3.1). 84.1% of estimates for sub-debris melt are within the grey shaded band. b) The percent contribution of ice cliffs to mass loss (sub-debris + ice cliff) with elevation. The red band contains the extreme range of melt contributions from ice cliffs. c) The fractional area of ice cliffs.

S3.1.3 Allowing ice cliff backwasting rates to vary with elevation in the ‘best case’

Here, we apply a linearly varying ice cliff backwasting rate with elevation. We apply the best fit linear curve through the median values of ice cliff backwasting rate in Fig. S7c. For this curve fit, the y-intercept is 13.94 cm d^{-1} and slope $-0.0123 \text{ cm (dm)}^{-1}$. For the ice cliff backwasting uncertainty we perturbed the linear fit ± 1 standard deviations of 2.46 cm d^{-1} . Except for the change in how ice cliff backwasting is represented all other parameters are the same as the ‘best case.’ The difference between this case and the original ‘best case’ is small (Table S3) and melt is not maximized in the *ZMT*.

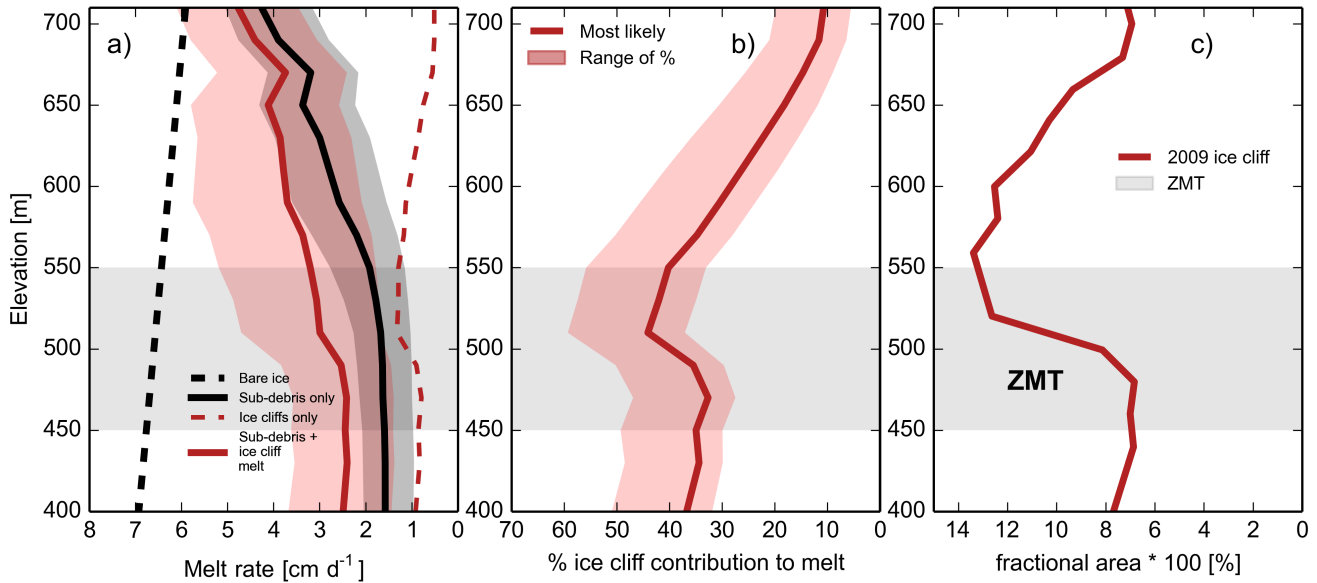


Fig. S17 The best distributed melt rate estimate with ice cliff backwasting rates that vary with elevation. ± 1 st. dev. bounds are applied to backwasting rate, mean ice cliff slope, and sub-debris melt. The red band contains an extreme range of sub-debris plus ice cliff melt based on compounding parameter choices such that 98.4 % of estimates lie within it (see section 2.3.1). 84.1% of estimates for sub-debris melt are within the grey shaded band. b) The percent contribution of ice cliffs to mass loss (sub-debris + ice cliff) with elevation. The red band contains the extreme range of melt contributions from ice cliffs. c) The fractional area of ice cliffs.

S3.2 Linear curve fits applied to each medial moraine individually

For completeness, we also explore the effect of applying a linear curve fit through debris thickness measurements for each medial moraine individually. The most likely outcome for this is shown in Figure S18.

As for the case above: For medial moraine #9 on the far western portion of the glacier, where access was difficult we apply a uniform debris thickness across the medial moraines (20 ± 10 cm; Fig. S14). Uncertainty bounds were not made in this case as linear curve fits through the interquartile range bounds produce negative debris thicknesses. The difference between this case and the original 'best case' is small (Table S3) and melt is not maximized in the ZMT.

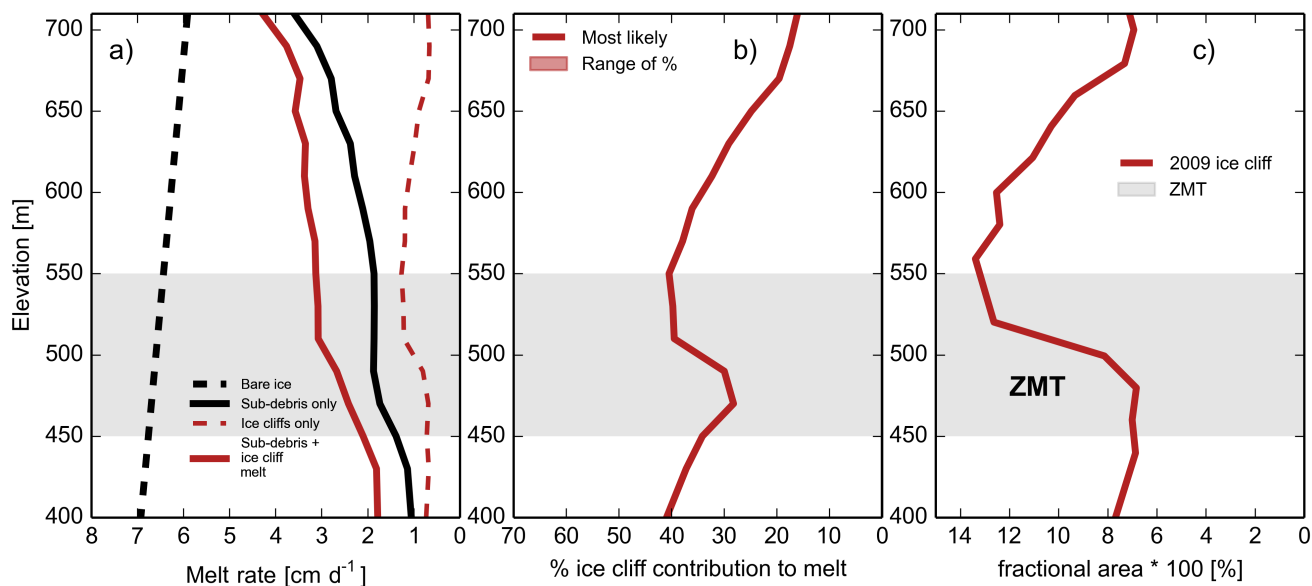


Fig. S18 Distributed melt estimates if a linear curve fit is applied to each individual medial moraine.

S3.3 A single, sigmoidal debris thickness-elevation curve across all medial moraines

We also explore the application of a single, sigmoidal debris thickness-elevation curve across all nine medial moraines. Note that the estimates presented in this section of the supplementary materials produce the highest sub-debris melt rates of any of the cases explored. But the area-averaged melt rates are still not maximized within the zone of maximum thinning (*ZMT*), nor do they approach what bare ice melt rates that are expected to be at a similar elevation, even in the extreme uncertainty case.

We apply a sigmoidal curve fit because it best matches the pattern of debris thickness with elevation using a root mean squared error (RMSE) metric (Fig. S19). This curve fit was produced using the median debris thickness from 50 m elevation bins producing an RMSE of 0.9 cm. The sigmoidal shape is able to represent the clear changes in slope of the median debris thickness (in 50 m bins) with elevation, while a linear curve fit is unable to capture this effect. The best fit linear curve produces an RMSE to the median debris thickness in 50 m elevation bins of 1.9 cm, twice as high as the sigmoidal curve fit.

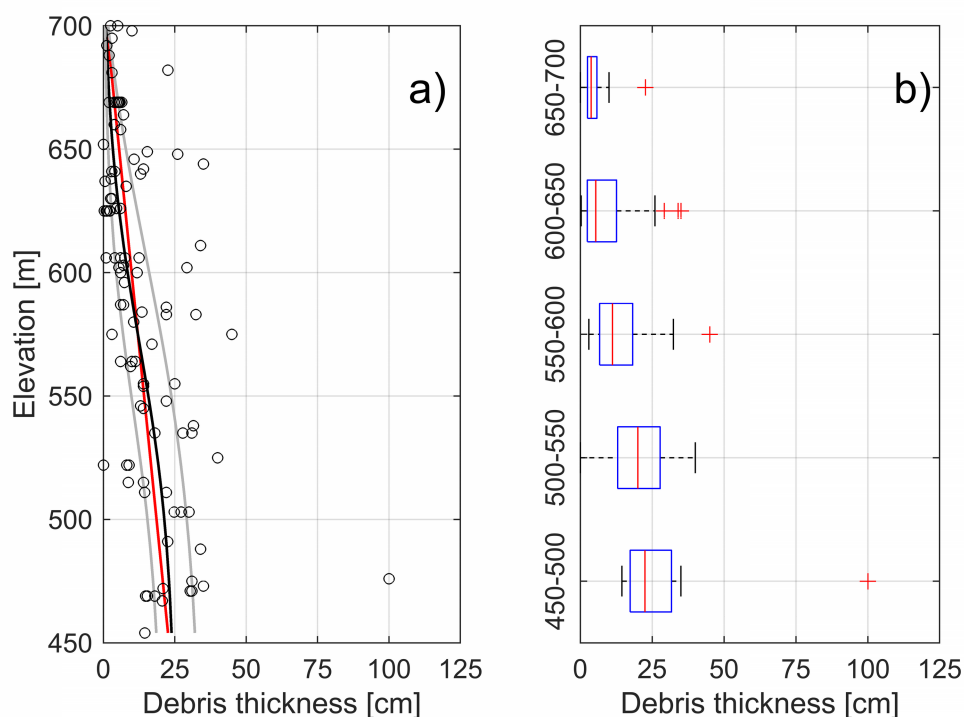


Fig. S19 Pattern of debris thickness with elevation across all medial moraines with sigmoidal and linear fits through the data. a) In situ debris thickness measurements with curve fits. With the sigmoidal curve fit to the 25% (grey), median (black), and 75% (grey) quartile debris thickness in 50 m bins. The points plotted are the mean debris thicknesses. The red line is the best linear fit. b) Debris thickness boxplots in 50 meter elevation bins. Outliers are represented as '+'s. The median measured debris thickness shows a non-linear shape when binned with elevation. For that reason we use a debris thickness curve fit that is also non-linear.

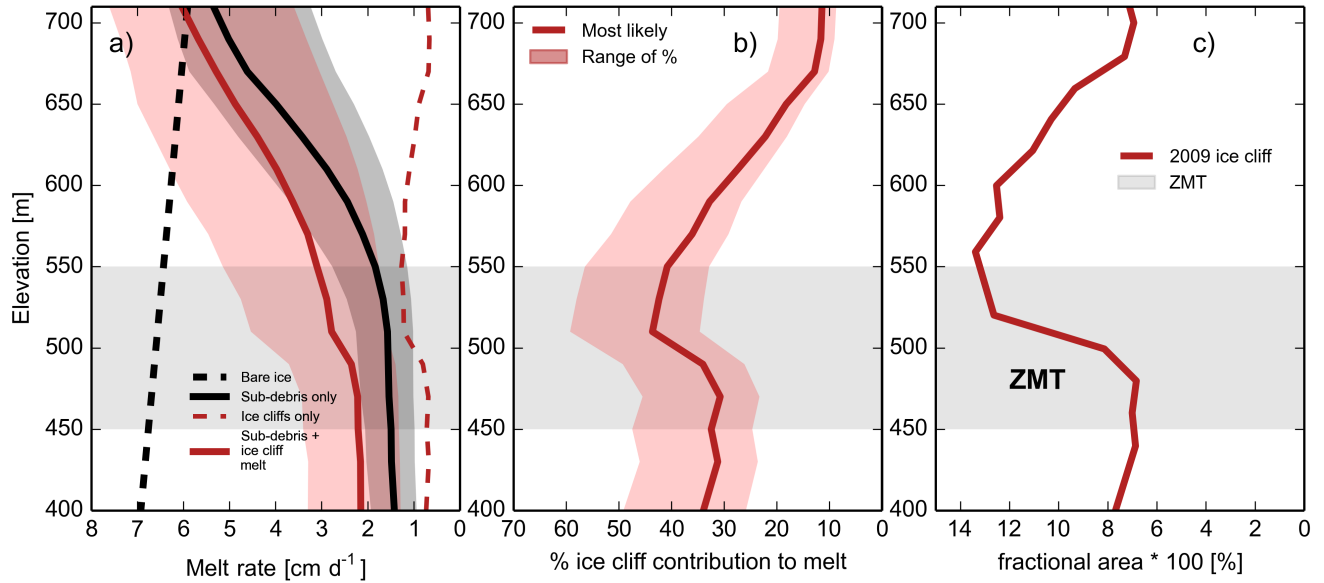


Fig. S20 The distributed melt rate estimate with a single sigmoidal curve fit applied across all medial moraines ± 1 st. Dev. bounds are applied to a uniform backwasting rate, the mean ice cliff slope, and the sub-debris melt. The red band contains an extreme range of sub-debris plus ice cliff melt based on compounding parameter choices such that 98.4 % of estimates lie within it (see section 2.3.1). 84.1% of estimates for sub-debris melt are within the grey shaded band. b) The percent contribution of ice cliffs to mass loss (sub-debris + ice cliff) with elevation. The red band contains the extreme range of melt contributions from ice cliffs. c) The fractional area of ice cliffs.

S4 Expansion of debris on Kennicott Glacier surface

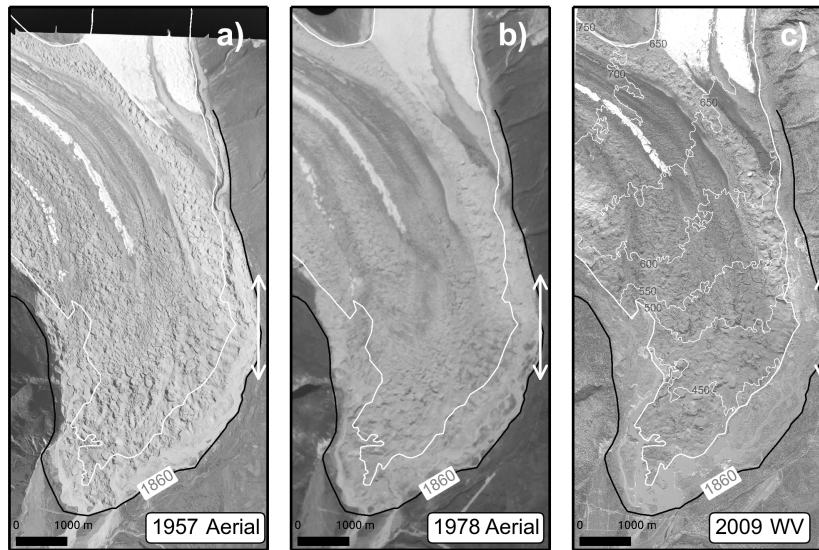


Fig. S21 Imagery of the Kennicott Glacier from 1957, 1978, and 2009, showing changes in the glacier surface through time. The arrows show the zone of maximum thinning (*ZMT*) between 1957 and 2004. The *ZMT* has been continuously debris covered since at least 1957. a) Aerial photo from July 29 1957 (courtesy of the USGS). b) Aerial photo from 25 August 1978 (courtesy of the USGS). The darkening of the glacier surface on the western portion of the glacier in the 1978 image may represent an increase in ice cliffs or a change in illumination angle. c) WorldView image from 13 July 2009 (catalog ID: 1020010008B20800) . Note the expansion of debris upglacier in time, especially in the western and central parts of the study area.

S5 Supplemental References

- Armstrong, W. H., Anderson, R. S., Allen, J. and Rajaram, H.: Modeling the WorldView-derived seasonal velocity evolution of Kennicott Glacier, Alaska, *Journal of Glaciology*, 62(234), 763–777, doi:10.1017/jog.2016.66, 2016.
- Brock, B. W., Mihalcea, C., Kirkbride, M. P., Diolaiuti, G., Cutler, M. E. J. and Smiraglia, C.: Meteorology and surface energy fluxes in the 2005–2007 ablation seasons at the Miage debris-covered glacier, Mont Blanc Massif, Italian Alps, *Journal of Geophysical Research*, 115(D9), doi:10.1029/2009JD013224, 2010.
- Brun, F., Buri, P., Miles, E. S., Wagnon, P., Steiner, J., Berthier, E., Ragetli, S., Kraaijenbrink, P., Immerzeel, W. W. and Pellicciotti, F.: Quantifying volume loss from ice cliffs on debris-covered glaciers using high-resolution terrestrial and aerial photogrammetry, *Journal of Glaciology*, 62(234), 684–695, doi:10.1017/jog.2016.54, 2016.
- Brun, F., Wagnon, P., Berthier, E., Shea, J. M., Immerzeel, W. W., Kraaijenbrink, P. D. A., Vincent, C., Reverchon, C., Shrestha, D. and Arnaud, Y.: Ice cliff contribution to the tongue-wide ablation of Changri Nup Glacier, Nepal, central Himalaya, *The Cryosphere*, 12(11), 3439–3457, doi:10.5194/tc-12-3439-2018, 2018.
- Conway, H. and Rasmussen, L. A.: Summer temperature profiles within supraglacial debris on Khumbu Glacier, Nepal, vol. 264, pp. 89–97, IAHS, Seattle, Washington., 2000.
- Crump, S. E., Anderson, L. S., Miller, G. H. and Anderson, R. S.: Interpreting exposure ages from ice-cored moraines: a Neoglacial case study on Baffin Island, Arctic Canada, *Journal of Quaternary Science*, 32(8), 1049–1062, doi:10.1002/jqs.2979, 2017.
- Fujita, K. and Sakai, A.: Air temperature environment on the debris-covered area of Lirung Glacier, Langtang Valley, Nepal Himalayas, in *Debris-Covered Glaciers*, vol. 264, p. 6, IAHS Publ., Seattle, Washington., 2000.
- Han, H., Wang, J., Wei, J. and Liu, S.: Backwasting rate on debris-covered Koxkar glacier, Tuomuer mountain, China, *Journal of Glaciology*, 56(196), 287–296, doi:10.3189/002214310791968430, 2010.
- Hock, R.: Temperature index melt modelling in mountain areas, *Journal of Hydrology*, 282(1–4), 104–115, doi:10.1016/S0022-1694(03)00257-9, 2003.
- Juen, M., Mayer, C., Lambrecht, A., Wirbel, A. and Kueppers, U.: Thermal properties of a supraglacial debris layer with respect to lithology and grain size, *Geografiska Annaler: Series A, Physical Geography*, 95(3), 197–209, doi:10.1111/geoa.12011, 2013.
- Kayastha, R. B., Takeuchi, Y., Nakawo, M. and Ageta, Y.: Practical prediction of ice melting beneath various thickness of debris cover on Khumbu Glacier, Nepal, using a positive degree-day factor, in *Debris-Covered Glaciers*, vol. 264, p. 11, IAHS Publ., Seattle, Washington., 2000.
- Kraaijenbrink, P. D. A., Shea, J. M., Pellicciotti, F., Jong, S. M. de and Immerzeel, W. W.: Object-based analysis of unmanned aerial vehicle imagery to map and characterise surface features on a debris-covered glacier, *Remote Sensing of Environment*, 186, 581–595, doi:10.1016/j.rse.2016.09.013, 2016.
- Loomis, S. R.: Morphology and ablation processes on glacier ice, *Proceedings of the Association of American Geographers*, 12, 88–92, 1970.
- MacKevett, E. M. Jr.: Geologic map of the McCarthy C-6 quadrangle, Alaska, 1972.
- MacKevett, E. M., Jr. and Smith, J. G.: Geologic map of the McCarthy B-6 Quadrangle, Alaska, 1972.

- Mihalcea, C., Mayer, C., Diolaiuti, G., Lambrecht, A., Smiraglia, C. and Tartari, G.: Ice ablation and meteorological conditions on the debris-covered area of Baltoro glacier, Karakoram, Pakistan, *Annals of Glaciology*, 43, 292–300, doi:10.3189/172756406781812104, 2006.
- Minder, J. R., Mote, P. W. and Lundquist, J. D.: Surface temperature lapse rates over complex terrain: Lessons from the Cascade Mountains, *Journal of Geophysical Research*, 115(D14), doi:10.1029/2009JD013493, 2010.
- Nakawo, M. and Young, G. J.: Field experiments to determine the effect of a debris layer on ablation of glacier ice, *Annals of Glaciology*, 2, 85–91, doi:10.3189/172756481794352432, 1981.
- Nakawo, M. and Young, G. J.: Estimate of glacier ablation under a debris layer from surface temperature and meteorological variables, *Journal of Glaciology*, 28(98), 29–34, 1982.
- Nicholson, L. and Benn, D. I.: Calculating ice melt beneath a debris layer using meteorological data, *Journal of Glaciology*, 52(178), 463–470, doi:10.3189/172756506781828584, 2006.
- Ohmura, A.: Physical basis for the temperature-based melt-index method, *Journal of Applied Meteorology*, 40(4), 753–761, 2001.
- Østrem, G.: Ice melting under a thin layer of moraine, and the existence of ice cores in moraine ridges, *Geografiska Annaler*, 41(4), 228–230, 1959.
- Owen, L. A., Derbyshire, E. and Scott, C. H.: Contemporary sediment production and transfer in high-altitude glaciers, *Sedimentary Geology*, 155(1–2), 13–36, doi:10.1016/S0037-0738(02)00156-2, 2003.
- Reid, T. D. and Brock, B. W.: Assessing ice-cliff backwasting and its contribution to total ablation of debris-covered Miage glacier, Mont Blanc massif, Italy, *Journal of Glaciology*, 60(219), 3–13, doi:10.3189/2014JoG13J045, 2014.
- Rickman, R. L. and Rosenkrans, D. S.: Hydrologic conditions and hazards in the Kennicott River Basin, Wrangell-St. Elias National Park and Preserve, Alaska, *Water-Resources Investigations Report*, U.S. Geological Survey, Anchorage, Alaska., 1997.
- Shaw, T. E., Brock, B. W., Fyffe, C. L., Pellicciotti, F., Rutter, N. and Diotri, F.: Air temperature distribution and energy-balance modelling of a debris-covered glacier, *Journal of Glaciology*, 1–14, doi:10.1017/jog.2016.31, 2016.
- Steiner, J. F. and Pellicciotti, F.: Variability of air temperature over a debris-covered glacier in the Nepalese Himalaya, *Annals of Glaciology*, 57(71), 295–307, doi:10.3189/2016AoG71A066, 2016.
- Watson, C. S., Quincey, D. J., Smith, M. W., Carrivick, J. L., Rowan, A. V. and James, M. R.: Quantifying ice cliff evolution with multi-temporal point clouds on the debris-covered Khumbu Glacier, Nepal, *Journal of Glaciology*, 63(241), 823–837, doi:10.1017/jog.2017.47, 2017.